



Cite this: *Chem. Commun.*, 2017, 53, 8691

Received 1st June 2017,
Accepted 7th July 2017

DOI: 10.1039/c7cc04218c

rsc.li/chemcomm

A new route for the synthesis of a Ag nanopore–inlay–nanogap structure: integrated Ag-core@graphene-shell@Ag-jacket nanoparticles for high-efficiency SERS detection†

Hengwei Qiu,^a Minqiang Wang,^{*a} Zhi Yang,^a Shouzhen Jiang,^b Yanjun Liu,^c Le Li,^a Minghui Cao^a and Junjie Li^a

We present a new route for the synthesis of Ag nanopore–inlay–nanogap structures using creviced graphene-shell encapsulated Cu nanoparticles (Cu@G-NPs) as the sacrificial templates. The as-synthesized integrated Ag-core@graphene-shell@Ag-jacket nanoparticles (AgC@G@AgJ-NPs) presents “chrysanthemum” shapes that contain abundant sub-10 nm size intraparticle nanopores/nanogaps, which can generate huge enhanced electromagnetic fields to support SERS activity, resulting in an average EF > 10⁷ due to a high-density of intraparticle and interparticle “hot spots”.

Noble-metal nanoparticles (NM-NPs) are able to generate intense electromagnetic fields in their vicinity due to their fascinating optical properties, *i.e.*, localized surface plasmon resonance (LSPR).¹ Surface-enhanced Raman scattering (SERS) is one of the most promising applications of such plasmonic effects, and produces Raman signals from surface-absorbed molecules that are enhanced by many orders of magnitude,² due to locally enhanced fields (so-called “hot spots”) where the electromagnetic field is extremely strong.³ The SERS activity of NM-NPs depends mainly on their shape, as this determines the number and position of hot spots and, therefore, it is critical to have a purposeful control over the shapes in order to maximise their performance.⁴ Typically, Ag nanoparticles (Ag-NPs) have been demonstrated to have excellent SERS activity,⁵ and they also can act as the sacrificial templates for the synthesis of other metal NPs, such as the synthesis of Au nanoboxes with a truncated cubic shape using sacrificial Ag cubes,⁴ and the synthesis of hollow Au–Ag alloy nanourchins using sacrificial Ag nanospheres.⁶ In order to maximize the SERS performance,

and to accommodate a variety of applications, great efforts have been made towards the creation of a high-density of hot spots using the rational design of Ag-NP structures. Over the past decade, Ag-NPs have been successfully synthesized in a great many diverse shapes⁷ including spheres,⁸ bars,⁹ plates,¹⁰ cubes,¹¹ tetrahedra,¹² octahedra,¹³ decahedra,¹⁴ and pentagonal rods/wires.¹⁵

Recently, in addition to the commonplace interparticle nanogaps, Ag-NPs with internal hot spots, such as those structures containing intraparticle nanogaps or nanopores, have been successfully fabricated, *e.g.*, nanocorals,¹⁶ nanostars,¹⁷ nanodendrites,¹⁸ and nanoflowers.¹⁹ Nanoporous structures have demonstrated significant strong local-field enhancement due to the combined effects of enhanced optical transmission and an intense electromagnetic field.²⁰ As a result of this strong local-field enhancement, abundant intraparticle nanopores can greatly promote the autologous SERS activity of a single particle, and serve to enhance the integral SERS sensitivity. Currently, some contradictory results relating to the influence of nanopore geometry and degree of porosity on the field enhancement are still existing,²¹ and the enhancement factor (EF) of the nanoporous structures is always weaker than that of other SERS substrates.²² The dimensional effect is particularly important for applications of nanoporous structures,²³ and only a few synthetic techniques can fabricate nanopores down to sub-10 nm. Beyond that, organic capping ligands are indispensable for the stabilization of conventional plasmonic nanoparticles with nanopores,²⁴ however these may prevent most probe molecules from accessing the hot spot regions and therefore greatly suppress the SERS activity.²⁵ Therefore, it is also a challenge to develop new synthetic strategies to ensure a clean and highly accessible nanoparticle surface for further enhancement of SERS activity.

In this work, we present a facile method to synthesize Ag-NPs that contain abundant sub-10 nm nanopores/nanogaps, integrated Ag-core@graphene-shell@Ag-jacket nanoparticles (AgC@G@AgJ-NPs), with intensive built-in hot spots. Our strategy briefly includes two nucleation and growth processes of Ag nanocrystals

^a Electronic Materials Research Laboratory (EMRL), Key Laboratory of Education Ministry, International Center for Dielectric Research (ICDR), School of Electronic and Information Engineering, Xi'an Jiaotong University, Xi'an 710049, China. E-mail: mqwang@mail.xjtu.edu.cn

^b School of Physics and Electronics, Shandong Normal University, Jinan 250014, China

^c Department of Electrical and Electronic Engineering, Southern University of Science and Technology, Shenzhen 518055, China

† Electronic supplementary information (ESI) available. See DOI: 10.1039/c7cc04218c

using creviced graphene-shell encapsulated Cu-core nanoparticles (Cu@G-NPs) as the sacrificial templates, without any organic capping ligands. The AgC@G@AgJ-NP array showed excellent SERS activity with an average EF > 10⁷ and good stability for long-term SERS detection.

Dual-temperature zone CVD technology was used to synthesize the sacrificial templates of Cu@G-NPs, which is a modified version of the method in our previous article (more details are shown in part 1 in the ESI†).²⁶ The field-emission scanning electron microscope (FESEM) image indicates that the Cu@G-NPs overall display a spherical shape with a smooth surface (Fig. S1b in ESI†), which can be attributed to the surface tension in the melting-solidification process. The transmission electron microscope (TEM) image shows the obvious contrast of the two successional components in a core@shell configuration in an individual Cu@G-NP with a size of 150 nm (Fig. S1d in ESI†). The magnified high-resolution TEM (HRTEM) image shows this core@shell configuration more clearly (Fig. S1e in ESI†), and the 0.35 nm distance between shell layers is in accordance with the interlayer spacing of graphite, suggesting the formation of a few-layer G-shell. In fact, each individual spherical G-shell is not continuous and seamless, but is composed of different graphene grains during the CVD process (an observed crevice is marked with the red rectangle in Fig. S1e in ESI†). Raman spectra can provide more information about the G-shell, and the presence of the G and 2D bands further prove the formation of a G-shell (Fig. S2 in ESI†).²⁷ Moreover, a strong D band in the Raman spectra indicates that abundant defects or disorder definitely exist in the crystal structure of the G-shell,²⁷ which is consistent with our foregoing analysis. The large curvature of the Cu@G-NP surface leads to the small grain-sizes and plentiful boundaries in the shell-surface, which give rise to the D band in Raman spectra. These breakages existing in the G-shell can act as multiple channels for the exchange of Ag ions and Cu atoms in the inside G-shell replacement reaction. The phase and purity of the sample were verified using X-ray diffraction (XRD) characterization (Fig. S3 in ESI†) and, obviously, the as-synthesized Cu-cores were crystallized in the face-centered cubic phase (*f*-cc, *Fm* $\bar{3}$ *m*, JCPDS no. 04-0836), and the clear and narrow (111), (200), (220), and (311) peaks indicate the high crystallinity of the Cu-cores. Furthermore, no peaks of impurities (including those of CuO, Cu₂O, *etc.*) can be observed in the XRD pattern, suggesting the high purity of the Cu@G-NPs.

The whole nanocasting processes proceeded with moderate stirring in a vacuum glove box (more details are shown in part 1 of the ESI†). After the pretreatment process in a FeCl₃ aqueous solution, spherical Cu@G-NPs with a relatively smooth surface and with particle sizes ranging from 40–120 nm and interparticle distances ranging from 50–150 nm were obtained (sample 1 in Fig. 1a and Fig. S4a, ESI†), and these are similar to the prodromic Cu@G-NPs without pretreatment. The difference between sample 1 and the prodromic Cu@G-NPs is the surface smoothness and, obviously, the prodromic Cu@G-NPs have a brighter and cleaner surface than sample 1. The rough areas on the surface as a result of the etching effect are the crevices in the G-shell (see the schematic in Fig. 1a), allowing Fe ions access during the pretreatment process. 20 min after the primary

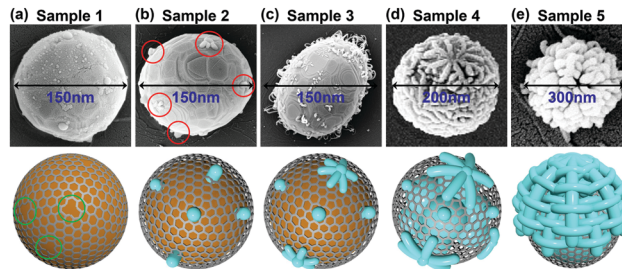


Fig. 1 FESEM images and schematics of the samples in different stages. (a) The samples after the pretreatment process, (b) samples with reaction times of 20 min, (c) 50 min, and (d) 3 h, and (e) the samples after the secondary nucleation and growth process.

growth process began, some short rod-like Ag “seeds” can be observed outside the G-shell (sample 2 in Fig. 1b). That some of the short rod-like Ag “seeds” share one centre indicates that only the crevices in the G-shell can act as sites for the reaction. With the reaction time increasing to 50 min, the short rod-like Ag “seeds” obviously become thicker and fatter (sample 3 in Fig. 1c and Fig. S4b, ESI†). The generation of Ag atoms finished after the inside-G-shell Cu atoms have been consumed and, subsequently, the primary growth process was complete when the system reached the first equilibrium state. After around 3 h since the replacement reaction began, the G-shell was encapsulated in the centre-radialized Ag-jacket (sample 4 in Fig. 1d and Fig. S4c, ESI†), forming the integrated three-tier structure of the AgC@G@AgJ-NPs (here we also call sample 4 the primary AgC@G@AgJ-NPs). It is worth noting that the whole reaction was proceeding in respectively independent regions, which can induce the multi-cores phenomenon inside the G-shell (we will discuss this phenomenon in combination with the TEM images below). As we know, the unique “ π ” band of graphene endows it with an excellent molecular affinity-surface for molecular adsorption,²⁸ which can trap probe molecules (especially aromatic molecules) into the outside G-shell nanogaps for high-efficiency detection. In order to intensify the efficacy of the outside G-shell nanogaps, we carried out a secondary nucleation and growth process using the reductant L-AA. When we added the L-AA solution dropwise in the excess AgNO₃ solution, the Ag ions were rapidly reduced to Ag atoms to obtain abundant supersaturated Ag atoms and, subsequently, nucleation and growth processes would happen. After the secondary nucleation and growth process (sample 5 in Fig. 1e and Fig. S4d, ESI†), the increment average size of AgC@G@AgJ-NPs can narrow the interparticle distance and deepen the nanogaps in the Ag-jacket.

The TEM image of sample 4 shows a clear contrast between the two interconnected components in the configuration before the secondary nucleation and growth process (Fig. 2a). Obviously, the inside Ag-core is divided into several parts due to the independent reaction sites in the G-shell, forming the conspicuous inside G-shell nanopores. It is interesting to note that, with the dispersive reaction sites as the channels for exchanging Ag ions and Cu atoms, many “bridges” between the inside G-shell Ag-core and outside G-shell Ag-jacket have been built during the growth process (marked with green arrows in Fig. 2a), which lead to this

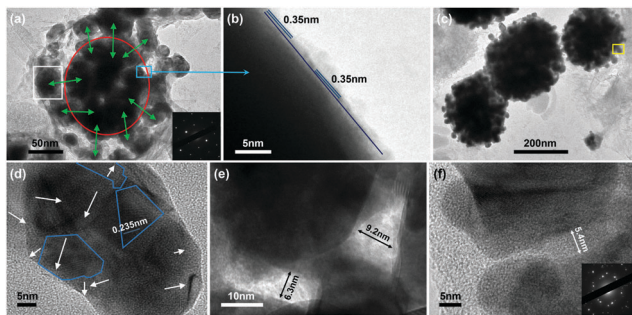


Fig. 2 TEM image (a) and HRTEM image (b) of an individual primary AgC@G@AgJ-NP (sample 4). TEM image (c) and HRTEM images (d–f) of the AgC@G@AgJ-NP (sample 5).

AgC@G@AgJ-NP as a whole. The electron diffraction pattern of a selected area shown in the inset (marked with a white box) of Fig. 2a indicates that the primary Ag-jacket in sample 4 has high crystallinity. The sandwich-type G-shell was investigated using a HRTEM image in an outside G-shell nanogap (Fig. 2b), and the clear contrast of the G-shell encapsulated Ag-core configuration can be observed, indicating the formation of the three-tier structure. In fact, the nanopore–inlay–nanogap structure was already formed in the primary AgC@G@AgJ-NPs. After the secondary nucleation and growth process, the outside G-shell nanogaps are narrowed down to sub-10 nm (sample 5 in Fig. 2c). Obviously, the sub-10 nm inside G-shell nanopores and outside G-shell nanogaps can structure the nanopore–inlay–nanogap configuration. The magnified HRTEM image from the yellow box area in Fig. 2c provides further insight into the structure of a AgC@G@AgJ-NP (Fig. 2d) and, these irregularly shaped humps are obviously composed of many small building blocks. Herein, three different building blocks with apparent boundaries were selected for investigation and it was found that each of them has its own crystallographic orientation due to the orientated attachment or grain rotation of the building units during the secondary growth process. In agreement with the XRD pattern (red curve in Fig. S5 in the ESI[†]), a lattice spacing of 0.235 nm can be observed in the HRTEM image, which is consistent with the *d* spacing of the (111) facet of a Ag nanocrystal. The sub-10 nm size of the nanopores/nanogaps is one of the most important characteristics of the AgC@G@AgJ-NPs, and the typical structural features were demonstrated using HRTEM images (Fig. 2e and f). The two randomly selected inside G-shell nanopores present a slit shape with size of 6.3 and 9.2 nm (Fig. 2e), and the nanoscale distance of the adjacent nanopores can also be very useful in the promotion of SERS activity. Additionally, a randomly selected outside G-shell nanogap in the Ag-jacket also presents a canyon configuration with a size of 5.4 nm (Fig. 2f). A small angle lattice mismatch between the building units can be observed in the electron diffraction pattern (inset in Fig. 2f), indicating some small transformations have happened in the crystallographic orientation during the orientated attachment process. That the particle-mediated aggregation process is leading the Ag nanocrystal growth kinetics rather than the atom-mediated classical crystallization process can be observed in the HRTEM images, and this is

consistent with the published works (more details are shown in part 3 ESI[†]).²⁹ The G-shell acts either as the micro reaction cavity for the inside replacement reaction, or as the growth template for the outside redox reaction. Moreover, it may, as the molecule enricher, solidly immobilize the probe molecules in the intraparticle hot spots areas. The structural stability of AgC@G@AgJ-NPs benefits from the separation effect of the Ag-cores and Ag-jacket. Furthermore, the mutually independent outside G-shell frameworks (*i.e.* the Ag-jacket in the primary AgC@G@AgJ-NPs) for the secondary growth process can prevent the building blocks of the Ag-jacket from clustering, endowing the outside G-shell Ag-jacket with a stable structure.

A kind of widely used probe molecule, Rhodamine 6G (R6G), was detected at ultralow concentrations (10^{-10} M) to evaluate the SERS sensitivity of the AgC@G@AgJ-NPs (more details are shown in part 1 of the ESI[†]). An apparent trend of increasing SERS intensity from sample 1 to sample 5 is observed (Fig. 3a). In particular, the signal intensities for the 615 cm^{-1} peak are found to increase by 1 : 3.1 : 10.4 : 45.6 : 69.6 for the nanoparticle arrays of samples 1, 2, 3, 4, and 5, respectively. It is therefore clear that, compared with sample 1 (Cu@G-NPs), sample 2 or 3 (Ag/Cu@G@Ag-NPs) and sample 4 (primary AgC@G@AgJ-NPs), sample 5 (AgC@G@AgJ-NPs) is superior for promoting high SERS activity due to the prominent intraparticle hot spots. The FESEM image (Fig. 3b) and optical microscopy image (Fig. 3c) in an expansive area reflect the uniformity of the AgC@G@AgJ-NP array (also shown in Fig. S7, ESI[†]). In accordance with the uniform distribution of the AgC@G@AgJ-NPs, the SERS response for point by point scanning mode (an area of $20 \times 20\ \mu\text{m}^2$) using a $\times 100$ objective lens and a $0.5\ \mu\text{m}$ step-size also displays a uniform Raman intensity at the 615 cm^{-1} peak (Fig. 3d). The whole scanning area includes 40×40 points and the whole scanning time was around 10 h; overall, the uniform intensity indicates the stability of the AgC@G@AgJ-NPs for continuous SERS detection. In order to describe the feasibility for long-term detection, we carried out a continuous monitoring experiment for 1200 s, and the very low amount of fluctuation indicates the good stability of the AgC@G@AgJ-NPs (more details are shown in Fig. S8, ESI[†]). Raman spectra collected from the scanning line along the red arrow line (all of the nanoparticles in this red scanning line are in the medium size range) in Raman mapping show corresponding increases of 1 : 1.04 : 1.07 : 1.14 : 1.13 : 1.10 : 1.05 at the 615 cm^{-1}

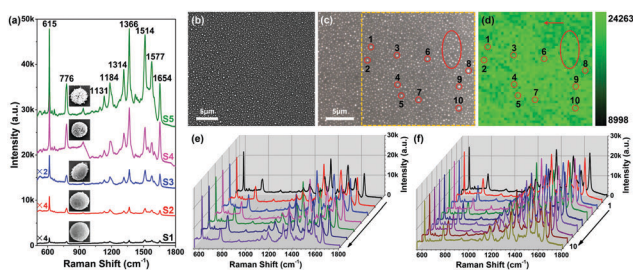


Fig. 3 (a) Raman spectra collected on the different substrates (samples 1–5). FESEM image (b), optical image (c), and Raman mapping (d) of the AgC@G@AgJ-NPs. (e) Raman spectra obtained along with the red arrow line. (f) Raman spectra obtained from the points marked with numbers 1–10.

peak (Fig. 3e). In these seven Raman spectra, the relative intensity at the 615 cm^{-1} peak fluctuates between 21 000–24 000 counts, and the intensity at the 1366 cm^{-1} peak fluctuates between 20 000–25 000 counts (Fig. S9a in the ESI[†]), indicating the good uniformity of the intensity distribution. Fig. 3f shows the 3D waterfall plot of the Raman spectra collected from the relatively large nanoparticles (marked with number 1–10 in Fig. 3c and d). In these ten Raman spectra, the relative intensity at the 615 cm^{-1} peak fluctuates between 22 000–25 000 counts with an average standard deviation (D) of 5.8%, and the intensity at the 1366 cm^{-1} peak fluctuates between 22 000–26 000 counts with an average D of 7.5% (more details are shown in Fig. S9b and Table S1 in the ESI[†]). Following the calculations and some assumptions described in previous reports (more details are shown in part 4 of the ESI[†]), the average EF of the AgC@G@AgJ-NPs for R6G detection can be as high as 10^7 orders of magnitude.

In summary, we present a facile route for the synthesis of a new type of nanopore-inlay-nanogap AgC@G@AgJ-NPs for Raman signal amplification with high uniformity and stability. The high uniformity of the SERS signal for continuous and long-term detection can promote the potential of the AgC@G@AgJ-NPs to be applied in ultralow concentration detection for drug security, food safety, environmental protection, *etc.* Compared with some other synthesis methods of nanopore/nanogap NM-NPs, our synthesis method does not need any organic capping ligands and is easy to be implemented.

The authors gratefully acknowledge financial support from the Natural Science Foundation of China (NSFC, Grant No. 51572216 and 61604122), the NSFC Major Research Program on Nanomanufacturing (Grant No. 91323303), the industrial science and technology research project in Shaanxi province (2015GY005) and the 111 Program (No. B14040). We sincerely thank Prof. Luyi Sun in the University of Connecticut, for his helpful discussions. The SEM and TEM work was done at the International Center for Dielectric Research (ICDR), Xi'an Jiaotong University, Xi'an, China.

Notes and references

- (a) S. Schlucker, *Angew. Chem., Int. Ed.*, 2014, **53**, 4756–4795; (b) S. Nie and S. R. Emory, *Science*, 1997, **275**, 1102–1106.
- (a) M. Fleischmann, P. J. Hendra and A. J. McQuillan, *Chem. Phys. Lett.*, 1974, **26**, 163–166; (b) J. F. Li, X. D. Tian, S. B. Li, J. R. Anema, Z. L. Yang, Y. Ding, Y. F. Wu, Y. M. Zeng, Q. Z. Chen, B. Ren, Z. L. Wang and Z. Q. Tian, *Nat. Protoc.*, 2013, **8**, 52–65.
- (a) H. Xu, J. Aizpurua, M. Kall and P. Apell, *Phys. Rev. E: Stat. Phys., Plasmas, Fluids, Relat. Interdiscip. Top.*, 2000, **62**, 4318–4324; (b) M. G. Albrecht and J. A. Creighton, *J. Am. Chem. Soc.*, 1977, **99**, 5215–5217.
- Y. Sun and Y. Xia, *Science*, 2002, **298**, 2176–2179.
- S. Y. Ding, J. Yi, J. F. Li, B. Ren, D. Y. Wu, R. Panneerselvam and Z. Q. Tian, *Nat. Rev. Mater.*, 2016, **1**, 16021.
- Z. Liu, Z. Yang, B. Peng, C. Cao, C. Zhang, H. You, Q. Xiong, Z. Li and J. Fang, *Adv. Mater.*, 2014, **26**, 2431–2439.
- Y. Xia, Y. Xiong, B. Lim and S. E. Skrabalak, *Angew. Chem., Int. Ed.*, 2009, **48**, 60–103.
- H. Liang, W. Wang, Y. Huang, S. Zhang, H. Wei and H. Xu, *J. Phys. Chem. C*, 2010, **114**, 7427–7431.
- B. J. Wiley, Y. Chen, J. M. McLellan, Y. Xiong, Z. Y. Li, D. Ginger and Y. Xia, *Nano Lett.*, 2007, **7**, 1032–1036.
- Q. Zhang, Y. Hu, S. Guo, J. Goebel and Y. Yin, *Nano Lett.*, 2010, **10**, 5037–5042.
- Q. Zhang, W. Li, C. Moran, J. Zeng, J. Chen, L. P. Wen and Y. Xia, *J. Am. Chem. Soc.*, 2010, **132**, 11372–11378.
- J. Zhou, J. An, B. Tang, S. Xu, Y. Cao, B. Zhao, W. Xu, J. Chang and J. R. Lombardi, *Langmuir*, 2008, **24**, 10407–10413.
- Y. Wang, D. Wan, S. Xie, X. Xia, C. Z. Huang and Y. Xia, *ACS Nano*, 2013, **7**, 4586–4594.
- B. Pietrobon and V. Kitaev, *Chem. Mater.*, 2008, **20**, 5186–5190.
- Y. Sun, B. Mayers, T. Herricks and Y. Xia, *Nano Lett.*, 2003, **3**, 955–960.
- L. Cheng, C. Ma, G. Yang, H. You and J. Fang, *J. Mater. Chem. A*, 2014, **2**, 4534–4542.
- A. Garcia-Leis, A. Torreggiani, J. V. Garcia-Ramos and S. Sanchez-Cortes, *Nanoscale*, 2015, **7**, 13629–13637.
- H. B. Li, P. Liu, Y. Liang, J. Xiao and G. W. Yang, *Nanoscale*, 2012, **4**, 5082–5091.
- H. Liang, Z. Li, W. Wang, Y. Wu and H. Xu, *Adv. Mater.*, 2009, **21**, 4614–4618.
- H. Rigneault, J. Capoulade, J. Dintinger, J. Wenger, N. Bonod, E. Popov, T. W. Ebbesen and P. F. Lenne, *Phys. Rev. Lett.*, 2005, **95**, 117401.
- L. H. Qian, X. Q. Yan, T. Fujita, A. Inoue and M. W. Chen, *Appl. Phys. Lett.*, 2007, **90**, 153120.
- Q. M. Yu, P. Guan, Q. Dong, G. Golden and P. M. Wallace, *Nano Lett.*, 2008, **8**, 1923–1928.
- B. M. Venkatesan and R. Bashir, *Nat. Nanotechnol.*, 2011, **6**, 615–624.
- D. R. Bae, S. J. Chang, Y. S. Huh, Y. K. Han, Y. J. Lee, G. R. Yi, S. Kim and G. J. Lee, *J. Nanosci. Nanotechnol.*, 2013, **13**, 5840–5843.
- Y. Yin and A. P. Alivisatos, *Nature*, 2005, **437**, 664–670.
- S. Xu, B. Man, S. Jiang, J. Wang, J. Wei, S. Xu, H. Liu, S. Gao, H. Liu, Z. Li, H. Li and H. Qiu, *ACS Appl. Mater. Interfaces*, 2015, **7**, 10977–10987.
- (a) X. Li, W. Cai, J. An, S. Kim, J. Nah, D. Yang, R. Piner, A. Velamakanni, I. Jung, E. Tutuc, S. K. Banerjee, L. Colombo and R. S. Ruoff, *Science*, 2009, **324**, 1312–1314; (b) A. C. Ferrari, J. C. Meyer, V. Scardaci, C. Casiraghi, M. Lazzeri, F. Mauri, S. Piscanec, D. Jiang, K. S. Novoselov, S. Roth and A. K. Geim, *Phys. Rev. Lett.*, 2006, **97**, 187401.
- (a) W. Xu, N. Mao and J. Zhang, *Small*, 2013, **9**, 1206–1224; (b) W. Qin, X. Li, W. W. Bian, X. J. Fan and J. Y. Qi, *Biomaterials*, 2010, **31**, 1007–1016.
- (a) H. M. Zheng, R. K. Smith, Y. W. Jun, C. Kisielowski, U. Dahmen and A. P. Alivisatos, *Science*, 2009, **324**, 1309–1312; (b) J. M. Yuk, J. Park, P. Ercius, K. Kim, D. J. Hellebusch, M. F. Crommie, J. Y. Lee, A. Zettl and A. P. Alivisatos, *Science*, 2012, **336**, 61–64; (c) H. You and J. Fang, *Nano Today*, 2016, **11**, 145–167.